Journal of the Indian Society of Remote Sensing (November 2019) 47(11):1831–1845
https://doi.org/10.1007/s12524-019-01023-4

RESEARCH ARTICLE

Impacts of Large-Area Impervious Surfaces on Regional Land Surface Temperature in the Great Pearl River Delta, China

Yuling Ma[1,2] · Kun Yang[2,3] · Shaohua Zhang[1,2] · Mingchan Li[1,2]

Received: 26 February 2019 / Accepted: 8 July 2019 / Published online: 12 August 2019

Abstract

Rapid urbanization has led to an increase in urban land surface temperature (LST). In contrast to individual cities or megacity scale, urban agglomeration can increase LST in a continuous area due to decreasing or disappearing distance between cities. Thus, the impact of ISA on LST needs further understanding in the large scale of urban agglomerations. This study investigated the impacts of impervious surface area (ISA) on LST in urban agglomeration region. The distribution of ISA and LST of the Greater Pearl River Delta in 2015 was extracted using the Landsat 8 OLI and Aqua MODIS images. Next, the standard deviational ellipse methods were used to systematically analyze the spatial correlation of ISA and LST. Subsequently, the influences of ISA density and landscape pattern of ISA on LST were analyzed by various methods. The results showed that when the ISA density increased 10%, the daytime LST increased 0.46 °C at the density level lower than 70% and 0.55 °C at the density level higher than 70%, respectively. Likewise, when the ISA density increased 10%, the nighttime LST increased 0.285 °C at the density level lower than 70% and 0.39 °C at the density level higher than 70%, respectively. In addition, the results of correlation analysis indicated that landscape metrics of ISA and the density of ISA had significant correlation with the LST. However, the correlation was higher at daytime than at nighttime, due to the large terrain, complex environment and diverse surface cover types in the study area.

Keywords Impervious surface · Land surface temperature · Landscape pattern · Landscape metric · Great Pearl River Delta

Introduction

According to the World Urbanization Prospects released by the United Nations in 2014, 54% of the world's population lives in urban areas, and this number will reach 66% by 2050 (Science 2016). The accelerating urbanization process leads to rapid growth in the population and in the number of new buildings. Natural land surfaces are gradually replaced by impervious surface areas (ISAs), such as cement, asphalt, and concrete (Lo et al. 1997). The rapid growth in ISA changes the way of surface radiation and energy distribution. One of the biggest negative effects is the rise in urban land surface temperature (LST), which results in urban heat island effect (Huang et al. 2012; Chen and Sun 2013). Therefore, understanding the relationship between urban ISA and LST has profound implications for urban planning and construction and reducing LST to mitigate urban heat island effects (Kaloustian and Diab 2015; Noro and Lazzarin 2015; Zheng et al. 2016; Zhao et al. 2017).

Researchers have studied the impact of ISA expansion on the LST at individual city or megacity scale. Xu (2009, 2010) pointed out that there is a significant positive correlation between the ISA and the LST. Xian and Crane (2006 investigated the thermal characteristics of the Tampa Bay Basin and the Las Vegas urban area. The results showed that there is a positive correlation between the LST and the percentage of ISA. Weng et al. concluded that the

✉ Kun Yang
kmdcynu@163.com

✉ Shaohua Zhang
zsh_11@163.com

[1] School of Tourism and Geographic Science, Yunnan Normal University, Kunming 650500, China

[2] The Engineering Research Centre of GIS Technology in Western China, Ministry of Education, Yunnan Normal University, Kunming 650500, China

[3] School of Information Science and Technology, Yunnan Normal University, Kunming 650500, China

LST increased with the growth of the ISA (Weng et al. 2004, 2007; Weng and Lu 2008). While the extension of urban ISA will change the landscape component of the city, the landscape component determines the heat transfer relationship of the land surface and can directly affect the urban LST change. Gong et al. (2007) took Beijing as an example and indicated that the difference in LST is closely related to urban land use/land cover type and its spatial distribution. Yue and Li-Hua (2007) found that the more complex the urban land type is in spatial layout, the more obvious the difference in LST. Li et al. (2011) found that the configuration and composition of urban landscapes also have a significant impact on the urban heat island effect. Peng et al. (2016a, b) studied the effects of landscape component and construction on urban thermal environment. After finding that the spatial construction of urban landscape has an influence on LST, some studies analyzed the relationship between landscape pattern and LST using landscape metrics (Liu et al. 2017). The major cities in Beijing and Shanghai were studied, and the largest patch index (LPI), landscape shape index (LSI) and landscape agglomeration (CONTAG) were found to be significantly correlated with LST (Peng et al. 2016b; Zhou et al. 2011; Li et al. 2013; Sun 2012). Estoque et al. (2017) showed the size, shape complexity, and aggregation of the patches of ISA had significant relationships with mean LST, though aggregation had the most consistent strong correlation. Furthermore, in the relationship between the landscape pattern and the cooling effect of green space, some studies have found that the green space patch with simple shape and concentrated distribution has better cooling effect (Li et al. 2012; Xu et al. 2015).

Urban agglomeration (also known as city clusters) represents a group of cities having a compact spatial organization and close economic connections (Fang 2015). In contrast to individual cities, urban agglomeration can increase LST in a continuous area due to decreasing or disappearing distance between cities (Du et al. 2016; Zhou et al. 2016, 2018). The Pearl River Delta (PRD) is one of the fastest-changing urban agglomerations in China with the urbanization rate higher than 80% (Runpeng 2013). The problems and negative effects of the rise in regional LST are caused by the centralized distribution of ISA. In order to improve the urban ecological environment, it is necessary to reduce the urban LST in the future process of urbanization through adjusting urban agglomeration planning and optimizing urban functional layout. Zhang et al. (2017a) used the monthly time scale dataset to investigate the effect of land cover types on LST in the PRD urban agglomeration. Zhang et al. (2017b) studied the spatiotemporal distribution of the urban heat islands in the PRD urban agglomeration, which revealed the rapid expansion of the urban agglomeration led to an increase in the intensity and extent of the urban heat island. Rao et al. (2010) denoted that the increase in regional LST was caused by the rapid urbanization in the PRD region. Jiang (2007) analyzed the thermal landscape of the PRD urban agglomeration and its daily variation.

However, the impact of ISA on LST remained poorly understood in the large scale of urban agglomerations, since most previous efforts focused on a single city or a few big cities. Therefore, this study obtained the Landsat 8 OLI remote sensing image data of the Great Pearl River Delta (GPRD) in 2015 to extract the ISA information using combinational biophysical composition index (CBCI); subsequently, the MOD11A2 data were employed to reveal the LST data. Moreover, the landscape metrics and mean LST of each ISA density area were calculated. Finally, the quantitative relationship between the ISA and the LST was measured by the correlation analysis method. The results can be used to mitigate urban heat island and future urban agglomerations planning.

Study Area and Datasets

Study Area

The Great Pearl River Delta (GPRD) is located in the south-central part of Guangdong Province (21°30′–23°40′N, 112°12′–113°48′E (Fig. 1), which includes Hong Kong, Macau, Guangzhou, Shenzhen, Foshan, Dongguan, Zhongshan, Zhuhai, Jiangmen, Zhaoqing and Huizhou. The region has a subtropical monsoon climate with hot and rainy summers and mild and humid winters. Moreover, The GPRD has an annual average temperature of about 21–23 °C and an annual precipitation of 1500 mm. Furthermore, the landforms of the GPRD are dominated by plains and hills with an altitude less than 200 m. In 2015, the GPRD area was 56,000 km^2, occupying 0.6% of the national land area. In addition, the population was 58.74 million with an urbanization rate of 84.12%. Economically, the gross domestic product (GDP) of the GPRD was 6710.86 billion yuan, accounting for 9.73% of the national GDP (Urban Agglomeration in the Pearl River Delta Yearbook 2016).

Data and Preprocessing

In this study, we used 7 cloud-free Landsat 8 Operational Land Imager (OLI) images downloaded from United States Geological Survey (USGS). The employed images were acquired in 2015 (see Table 1). A Landsat 8 OLI image contains 11 bands, including eight multispectral (Bands 1–7 and 9), one panchromatic (Band 8) and two thermal (Bands 10 and 11) bands (Roy et al. 2014). We employed

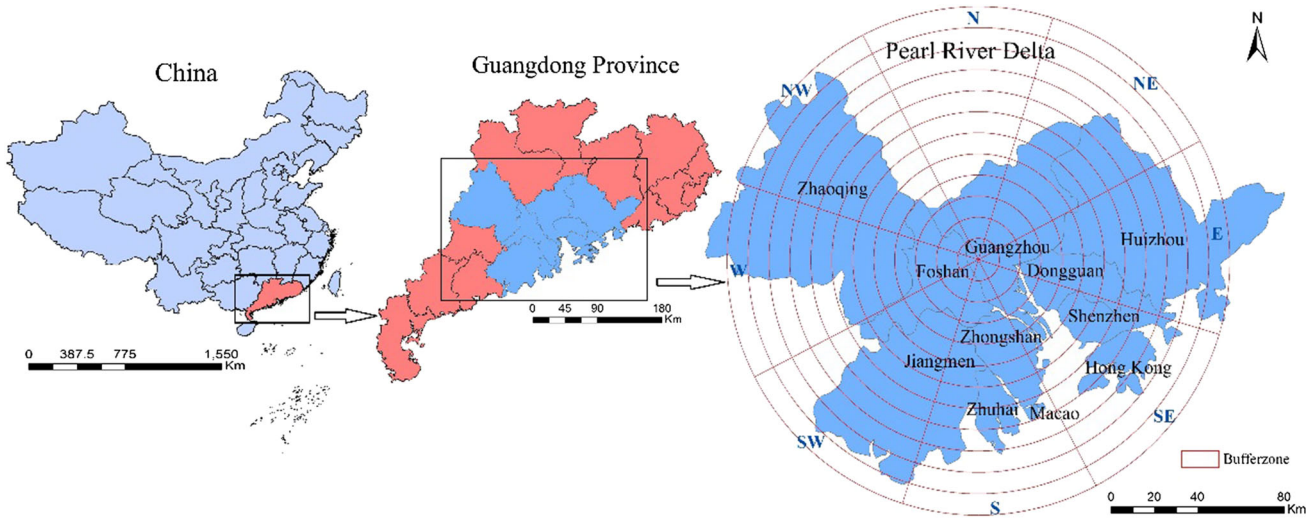

Fig. 1 Geographical location of the GPRD

Table 1 Description of the study data used

Landsat 8 scene ID	Acquisition date and time
(a) Landsat data for the study areas	
LC81210442015220LGN00	August 8, 2015; 02:45:34
LC81220432015291LGN00	October 18, 2015; 02:51:44
LC81220442015291LGN00	October 18, 2015; 02:52:08
LC81220452015291LGN00	October 18, 2015; 02:52:32
LC81230432015106LGN00	April 16, 2015; 02:57:17
LC81230442015106LGN00	April 16, 2015; 02:57:41
LC81230452015106LGN00	April 16, 2015; 02:58:04
MODIS scene ID (day and night)	MODIS scene ID (day and night)
(b) MODIS data for the study areas	
MOD11A2.A2015001	MOD11A2.A201500177
MOD11A2.A2015009	MOD11A2.A201500233
MOD11A2.A20150017	MOD11A2.A201500265
MOD11A2.A20150025	MOD11A2.A201500281
MOD11A2.A20150089	MOD11A2.A201500289
MOD11A2.A20150097	MOD11A2.A201500321
MOD11A2.A201500105	MOD11A2.A201500337
MOD11A2.A201500161	MOD11A2.A201500345

red, green and near-infrared bands with a spatial resolution of 30 m × 30 m. Data preprocessing includes geometric correction, radiometric calibration, flash atmospheric correction, band synthesis and study area cropping. In addition, the overall images processing and data analysis steps are shown in Fig. 2.

The Landsat 8 OLI images of the same day cannot be obtained due to the large study area. Therefore, the LST data of the study area were obtained by Terra MODIS 8-day composite products (MOD11A2) (http://ladsweb.nascom.nasa.gov/data/search.html) with a spatial resolution of 1 km × 1 km in 2015 (see Table 1). The LST data were retrieved from clear-sky (99% confidence) observations monitored at 10:30 h (daytime) and 22:30 h (nighttime) local solar time using a generalized split-window algorithm (Wan and Dozier 1996). The validation of the in situ LST data measurements indicates that the accuracy of MODIS LST data was better than 1 °C in most cases (Wan 2008). To eliminate the effects of extreme weather during the year, the study used the annual mean LST of the GPRD (day and night). We assigned the null value of the MODIS image to 0 and then calculate the annual mean LST. Furthermore, the LST unit was converted from kelvin to degree Celsius.

Methods

Impervious Surface Mapping

This study used the combined biophysical composition index (CBCI) to extract impervious surface information. The CBCI is an effective index for highlighting four major urban biophysical compositions (including impervious surface, vegetation, bare soil and water) and performs well in separating impervious surface and bare soil (Zhang et al. 2018).

$$\mathrm{CBCI} = \mathrm{MBSI} * (1 + A) - \mathrm{OSAVI} + A \quad (1)$$

where A is a correction factor, calculated by liner regression, which is employed to increase the value of the MBSI and decrease the value of the OSAVI. In this study, 0.51 was selected as the optimal value to enhance the discrimination of the impervious surfaces, bare soil, vegetation and water (Zhang et al. 2018).

We used modified bare soil index (MBSI) to discriminate bare soil from other land cover types.

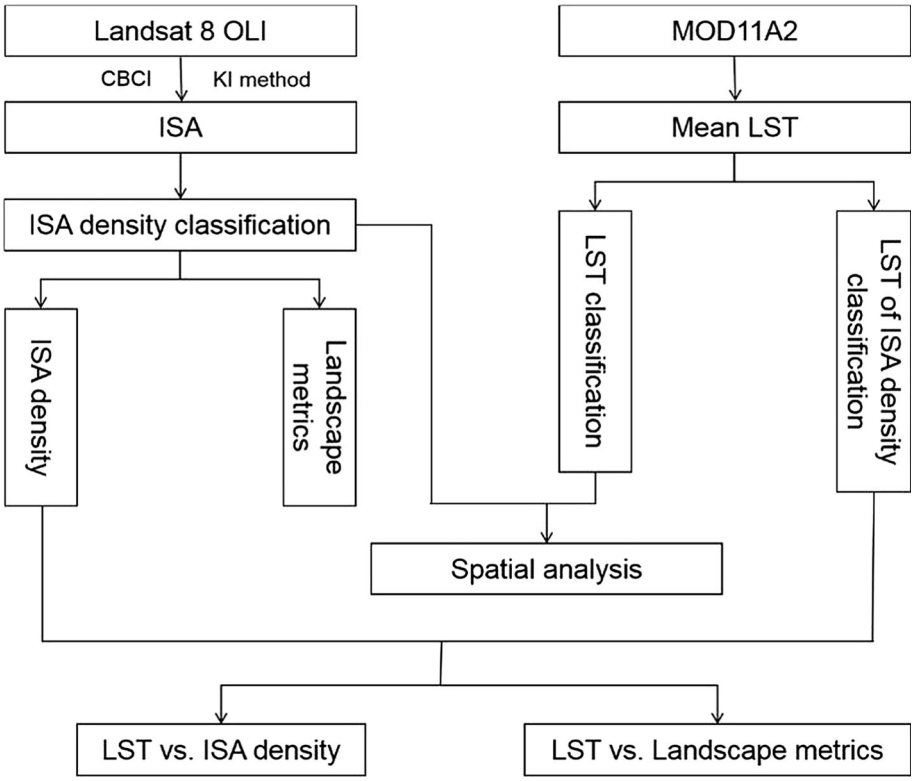

Fig. 2 Flowchart

$$\mathrm{MBSI} = \frac{(\mathrm{Red} - \mathrm{Green}) * 2}{(\mathrm{Red} + \mathrm{Green} - 2)} \quad (2)$$

where Red and Green are the reflectance of the red and green bands, respectively, and 2 is a correction factor which can be used to enhance the distinction of bare soil and the other three biophysical compositions.

In addition, the optimized soil-adjusted vegetation index (OSAVI) was carried out to enhance the vegetation information in remote sensing imagery (Rondeaux et al. 1996).

$$\mathrm{OSAVI} = \frac{\mathrm{NIR} - \mathrm{Red}}{\mathrm{NIR} + \mathrm{Red} + 0.16} \quad (3)$$

where NIR and Red are the reflectance of the near-infrared and red band, respectively.

The Kittler–Illingworth (KI) method was used in this study to select the optimal threshold (Kittler and Illingworth 1986). It assumes that the observations come from a mixture of two normal distributions having respective mean, variances and proportions. Given a brightness level as trial threshold, it models two resulting pixel populations: one from which the brightness level is smaller than the threshold and the other from the pixels whose brightness level is larger than the threshold (Kittler and Illingworth 1986; Sungzoon et al. 1989). The selected threshold values are shown in Table 2.

Table 2 CBCI threshold values selection

Landsat 8 scene ID	Threshold values
LC81210442015220LGN00	0.24–0.42
LC81220432015291LGN00	0.23–0.41
LC81220442015291LGN00	0.23–0.47
LC81220452015291LGN00	0.27–0.45
LC81230432015106LGN00	0.23–0.44
LC81230442015106LGN00	0.28–0.44
LC81230452015106LGN00	0.36–0.42

Landscape Metrics

The landscape pattern is the type, size, shape and spatial configuration of landscape patches (McGarigal et al. 2002). The landscape metric was used to characterize landscape patterns (Gustafson 1998; Jun Xiang et al. 2004; McGarigal and Marks 1995; Wu 2004) and to relate landscape patterns to ecological processes (Turner 2005). These metrics fall into two general categories to measure the component and spatial construction (Gustafson 1998; McGarigal and Marks 1995). The landscape component metrics measure the presence and amount of different patch types within the landscape, and the landscape construction metrics measure the spatial distribution of patches within the landscape (Alberti 2005). In this study, we selected

Table 3 Landscape pattern metrics used in this study

Landscape metrics	Description	Calculation
Number of patches (NP)	Describe the heterogeneity of the landscape, the more the number of patches, the more fragmented the landscape	$NP = N$
Patch density (PD)	The number of patches per unit area, describing patch fragmentation	$PD = \frac{n_i}{A}$
Landscape shape index (LSI)	Reflects the complex shape of the landscape. The larger the value, the more irregular the shape, the higher the landscape complexity and the lower the stability	$LSI = \frac{0.25E}{\sqrt{A}}$
Fractal dimension (PAFRAC)	The degree of complexity of the landscape type is shown. The smaller the value, the more the landscape shape tends to be square. The larger the value, the more complex the shape of the landscape is	$PAFRAC = \frac{2 \Big/ \left[n_i \sum_{i=1}^{n} \sum_{j=1}^{m} \left(\ln P_{ij} \times \ln A_{ij} \right) - \sum_{i=1}^{n} \sum_{i=1}^{m} \ln P_{ij} \sum_{i=1}^{n} \sum_{i=1}^{m} \ln A_{ij} \right]}{n_i \sum_{i=1}^{n} \sum_{j=1}^{m} \ln P_{ij}^2 - \sum_{i=1}^{n} \sum_{i=1}^{m} \ln P_{ij}}$
Largest patch index (LPI)	The proportion of the largest patch in a patch type to the entire landscape area. Reflect the degree of fragmentation. The larger the value, the larger the area of patch contiguity	$LPI = \frac{\max_{j=1}^{m}(a_{ij})}{A}$
Mean patch size (AREA_MN)	Characterize the degree of fragmentation of the landscape	$AREA_{MN} = \frac{A}{n_i} \times 10^6$
Landscape aggregation index (AI)	Reflect the non-randomness or degree of aggregation of different types of patches in the landscape. The smaller the value, the more discrete the landscape	$AI = \left[\sum_{i=1}^{n} \left(\frac{g_{ii}}{g_{ii\max}} \right) \times P_i \right] \times 100$
Path cohesion index (COHESION)	Reflecting the natural connectivity of landscape types, the higher the spatial connectivity of a certain type of landscape, the greater the metric	$COHESION = \left\{ \left[1 - \sum_{j=1}^{n} P_{ij} \Big/ \left(\sum_{j=1}^{n} P_{ij} \times a_{ij}^{1/2} \right) \right] \Big/ \left(1 - 1/A^{1/2} \right) \right\} \times 100$

In the formula, i = 1, 2, …, n is the landscape type serial number; j = 1, 2, …, m is the patch serial number; ni is the total number of patches whose landscape type is i; A is the landscape total area; aij is the largest patch area in a landscape type; gii is the number of neighboring pixels of the patch type i; giimax is the largest contiguous neighbor of the patch type i; Pi is the ratio of the area of a type i to the total area

eight commonly used landscape metrics to relate LST to landscape patterns (Table 3). These landscape metrics were calculated using Fragstats 4.2 software, employing the eight-neighbor rule (McGarigal et al. 2002).

LST Classification

The LST classification describes the LST distribution characteristics directly. The two commonly used methods were employed to divide LST, which were equal interval method and mean-standard deviation method (Zhang et al. 2006; Xu and Chen 2003; Zhang 2006). Previous studies have shown that mean-standard deviation method was better than equal interval method in describing LST spatial distribution and details (Chen and Wang 2009). Therefore, this study employed the mean-standard deviation method to divide the LST of daytime and nighttime into five groups (low-temperature zone, sub-middle-temperature zone, intermediate-temperature zone, sub-high-temperature zone and high-temperature zone). The details of the mean-standard deviation method are shown in Table 4.

Spatial Correlation Analysis

Spatial Analysis

The standard deviational ellipse (SDE) is thus a useful and versatile tool for spatial description, reflecting to some extent the overall contour and dominant distribution of point space organization (Gong 2002; Lefever 1926). The SDE consists of three elements: the rotation angle θ, the standard deviation along the major axis (long axis X) and

Table 4 Mean-standard deviation method

Thermal level	Brightness temperature range formula	Brightness temperature range	
		Daytime (°C)	Nighttime (°C)
Low-temperature zone	$Tb < \mu - std$	$Tb < 26.95$	$Tb < 21$
Sub-medium-temperature zone	$\mu - std \leq Tb < \mu - 0.5\ std$	$26.95 \leq Tb < 28.06$	$21 \leq Tb < 21.8$
Intermediate-temperature zone	$\mu - 0.5\ std \leq Tb \leq \mu + 0.5\ std$	$28.06 \leq Tb \leq 30.29$	$21.8 \leq Tb \leq 23.39$
Sub-high-temperature zone	$\mu + 0.5\ std < Tb \leq \mu + std$	$30.29 < Tb \leq 31.41$	$23.39 < Tb \leq 24.18$
High-temperature zone	$Tb > \mu + std$	$Tb > 31.41$	$Tb > 24.18$

In the table, μ is the average of the LST after normalization and std is the standard deviation of the standard LST

the standard deviation along the minor axis (short axis Y) (Fischer 2010). We calculated the SDE of the high-density area of the ISA density and the high-temperature zone of the LST in 2015, respectively. The formula for calculating the SDE is as follows:

$$x_i' = x_i - x_{\text{wmc}} \tag{4}$$

$$y_i' = y_i - y_{\text{wmc}} \tag{5}$$

$$\tan\theta = \frac{\left[\sum_{i=1}^{n} w_i^2 x_i'^2 - \sum_{i=1}^{n} w_i^2 y_i'^2\right] + \sqrt{\left(\sum_{i=1}^{n} w_i^2 x_i'^2 - \sum_{i=1}^{n} w_i^2 y_i'^2\right)^2 + 4\left(\sum_{i=1}^{n} w_i^2 x_i'^2 y_i'^2\right)^2}}{2\sum_{i=1}^{n} w_i^2 x_i'^2 y_i'^2} \tag{6}$$

$$\delta_x \sqrt{\frac{\sum_{i=1}^{n} (w_i x_i' \cos\theta - w_i y_i' \sin\theta)^2}{\sum_{i=1}^{n} w_i^2}} \tag{7}$$

$$\delta_y \sqrt{\frac{\sum_{i=1}^{n} (w_i x_i' \sin\theta - w_i y_i' \cos\theta)^2}{\sum_{i=1}^{n} w_i^2}} \tag{8}$$

where x_i' and y_i' are the relative coordinates of the center of gravity of each point distance region, and the corner of the point distribution pattern can be obtained according to tan θ. δ_x and δ_y are the standard deviation along the x-axis and the y-axis, respectively (Wong 1999). The above calculations can be implemented with ArcGIS 10.2.

Correlation Analysis

The Pearson's correlation coefficients between the landscape pattern metrics and LST were calculated using SPSS PASW Statistics 19 (SPSS Inc.).

$$r = \frac{1}{n-1} \sum_{i=1}^{n} \left[\frac{X_i - \bar{X}}{s_X}\right] \left[\frac{Y_i - \bar{Y}}{s_Y}\right] \tag{9}$$

where $\left[\frac{X_i - \bar{X}}{s_X}\right]$, $\bar{X}$ and s_X are standardized variables, sample mean and sample standard deviation, respectively.

Results

Spatial Distribution of ISA

The accuracies of the ISA maps were assessed by using the high-resolution images and pictures incorporated in Google Earth Pro. The "view historical imagery" tool in Google Earth Pro was used to find the best possible referenced image for 2015. This study randomly selected 100 verification sample points in the four regions of GPRD (Guangzhou, Foshan, Dongguan and

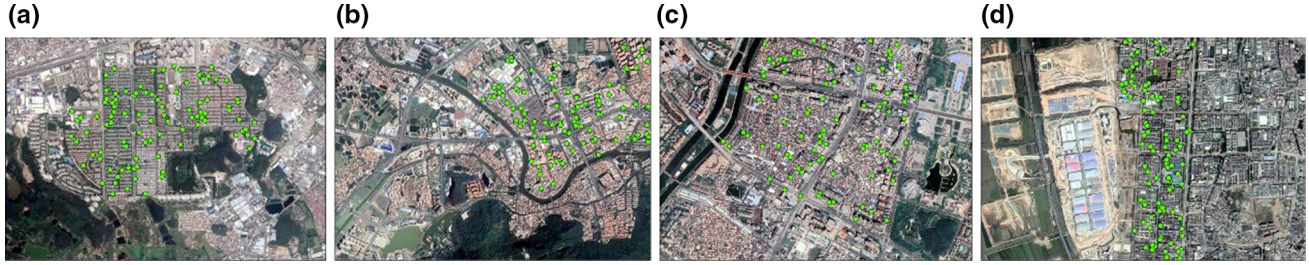

Fig. 3 Accuracy verification: **a** Guangzhou sample points, **b** Foshan sample points, **c** Dongguan sample points, **d** Shenzhen sample points

Table 5 Results of the accuracy verification

	Guangzhou	Foshan	Dongguan	Shenzhen
Total accuracy (%)	96.35	92.37	94.73	95.48
Kappa coefficient	0.9248	0.8920	0.9151	0.9336

Shenzhen) (Fig. 3) and used the confusion matrix method to verify the accuracy of the ISA extraction results. The results of the accuracy verification are shown in Table 5.

The impervious surface area (ISA) maps were obtained from the Landsat OLI data of 2015, with a spatial resolution of 30 m × 30 m. To be converted to density of the ISA, the ISA map resolution was resampled to 100 m × 100 m. Subsequently, the density of ISA was obtained by counting the sum number of ISAs within 10 × 10 pixels. We further stratified the ISA into five groups based on the ISA density. Emanating inward from the lowest to the highest ISA density in the GPRD (Fig. 4b), these five areas were low-density area, sub-medium-density area, medium-density area, sub-high-density area, and high-density area. The classification threshold values are shown in Table 6.

The ISA distribution of the GPRD in 2015 is shown in Fig. 4a. In 2015, the total amount of ISA was 9754.936 km^2, accounting for 17.4% of the GPRD. Moreover, a cluster pattern of the ISA distribution can be observed on the distribution map of ISA. The ISAs were mainly distributed in five cities of Foshan, Guangzhou, Dongguan, Shenzhen and Zhongshan, which have narrow traffic arteries along the coast. However, the northwest part of Zhaoqing and the northeast of Huizhou have a small proportion of ISA due to the restrictions of mountainous and hilly terrain. The graded ISA distribution map

Table 6 Classification threshold values

ISA classification	ISA density (%)
Low-density area	< 20
Sub-medium-density area	20–45
Medium-density area	45–70
Sub-high-density area	70–90
High-density area	> 90

(Fig. 4b) shows that the high-density area of ISA was clustered in the border area between Foshan and Guangzhou and also in Shenzhen, Zhongshan and Dongguan, with a coverage rate of over 90%. The density of ISA decreases gradually from the central region to the marginal region.

Changes in Landscape Metrics of Different Percent ISAs

The characteristics of landscape metrics of five ISA density areas are shown in Table 7 and Fig. 5, which shows that according to trends in ISA density changes, the NP and PD demonstrate a progressive decline, having significant and negative correlation with ISA density. The values of LSI and PAFRAC increased first and then decreased with trends in ISA density changes. The LSI has the largest value in the sub-medium-density area, indicating that the patches are discrete and irregular in these areas. In addition, when the value of PAFRAC approaches 1, the patches shape is regular and the patches dissociate as the value approaches 2. In the medium-density area, the PAFRAC value was closest to 2, denoting that the patches were dispersed and the patches shape was irregular. Moreover,

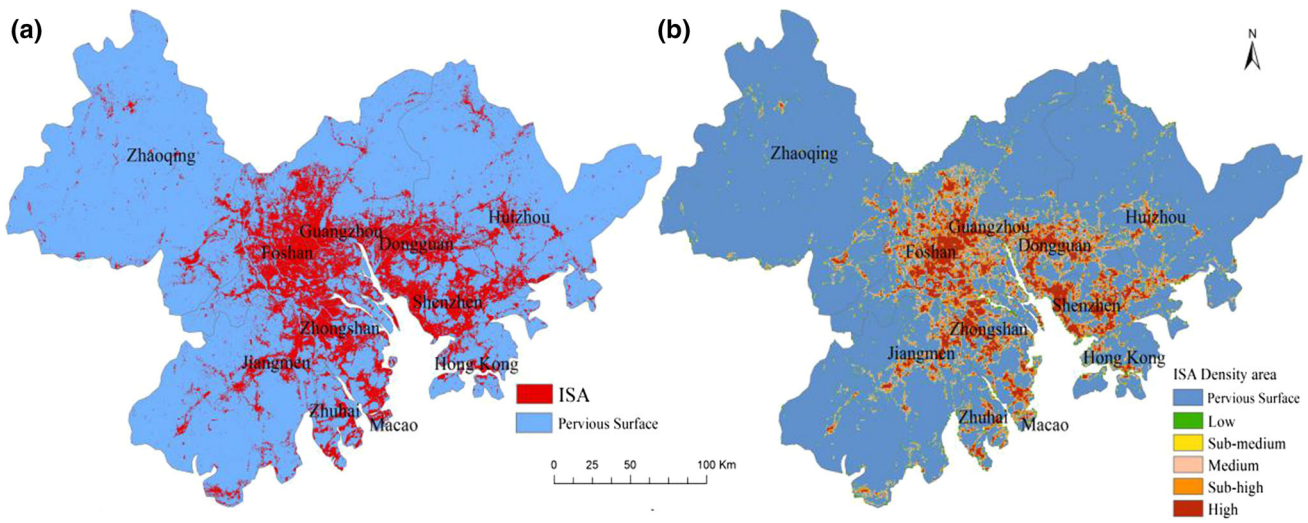

Fig. 4 **a** ISA map: **b** classification map for ISA

Table 7 Landscape metrics statistics

	Low-density area	Sub-medium-density area	Medium-density area	Sub-high-density area	High-density area
NP	1656	1471	1121	722	338
PD	0.013	0.012	0.009	0.006	0.003
LSI	46.43	50	44.98	38.82	24.18
PAFRAC	1.66	1.67	1.69	1.68	1.51
LPI	0.013	0.03	0.03	0.07	0.52
AREA_MN (ha)	290.09	296.13	314.81	426.04	917.46
AI	91.55	92.56	92.58	93.16	95.83
COHESION	93.41	95.69	96.01	97.00	98.71

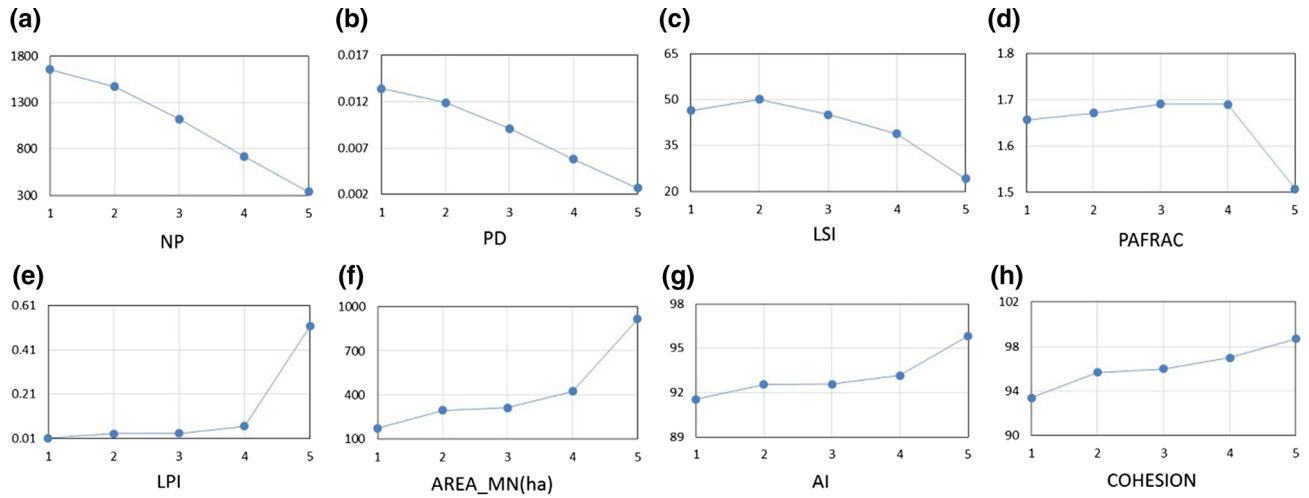

Fig. 5 Landscape metrics trend map: **a** NP, **b** PD, **c** LSI, **d** PAFRAC, **e** LPI, **f** AREA_MN, **g** AI, **h** COHESION

the LPI, AREA_MN, AI, COHESION were positively correlated with ISA density.

In general, as the density of the ISA increases, the voids of the patches decrease such that the single patch area increases and the connectivity between the patches is strong. In addition, the patch shape tends to be regular.

Spatial Distribution of LST

In the GPRD, the annual average daytime LST was 22.68–37.56 °C and the nighttime LST was 15.84–26.74 °C in 2015 (see Fig. 6). The temperature difference of daytime and nighttime is 14.88 °C and 10.9 °C, respectively. The high-temperature zone of daytime (defined here as LST $\geq$ 31.41 °C is high-temperature zone) was clustered distribution at the core area of GPRD, mainly distributed in Foshan, Guangzhou, Dongguan, Zhongshan and Shenzhen. The high-temperature zone and the low-temperature zone have significant value of the temperature difference. On the contrary, the spatial extent of high-temperature zone of nighttime was larger than that of daytime. The high-temperature zones almost cover the central region of the GPRD, except for parts of Zhaoqing, Huizhou and Jiangmen (Figure 7). This phenomenon is mainly because the study area is adjacent to the ocean, which is affected by water thermal insulation at night, and the high-temperature zone is larger than at the daytime.

However, regardless of daytime or nighttime, the high-density area of ISA is usually the core area of high-temperature zone, such as Guangzhou, Foshan, Zhongshan and Jiangmen, which are all the central areas of high-temperature zone. In addition, the larger the proportion of high-density area of ISA is, the more obvious the phenomenon of high LST value is. Likewise, the phenomenon of high LST value is not obvious in the northwest and northeast due to the small proportion of the ISA.

SDE of ISA and LST Classification

In the SDE map (Fig. 8), the direction of the long axis and the short axis represent the direction of the data distribution and the range of the data distribution,

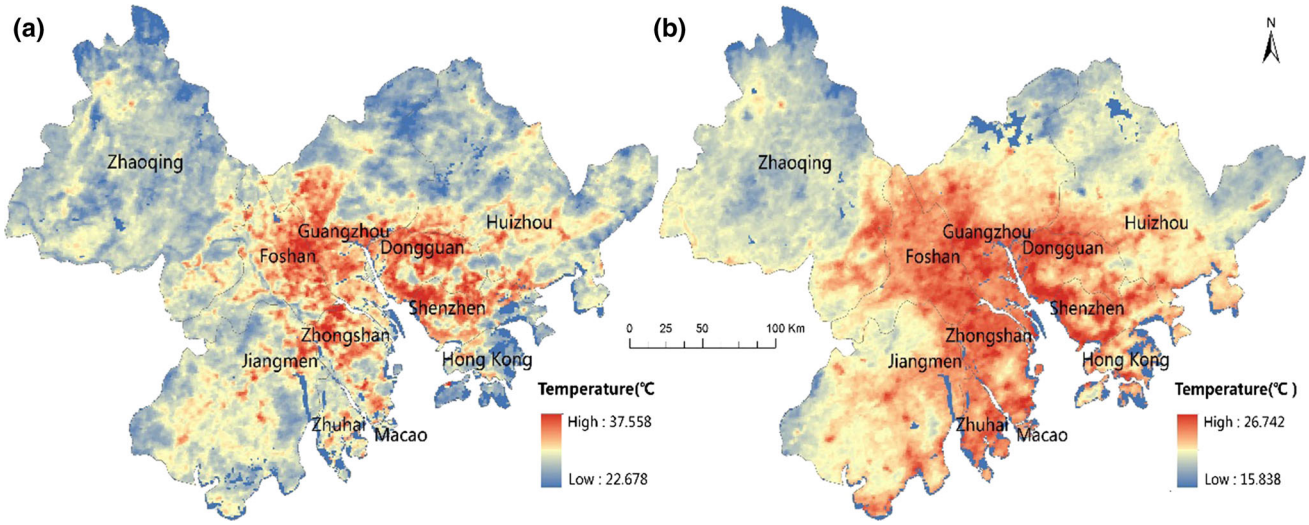

Fig. 6 LST distribution map: **a** day, **b** night

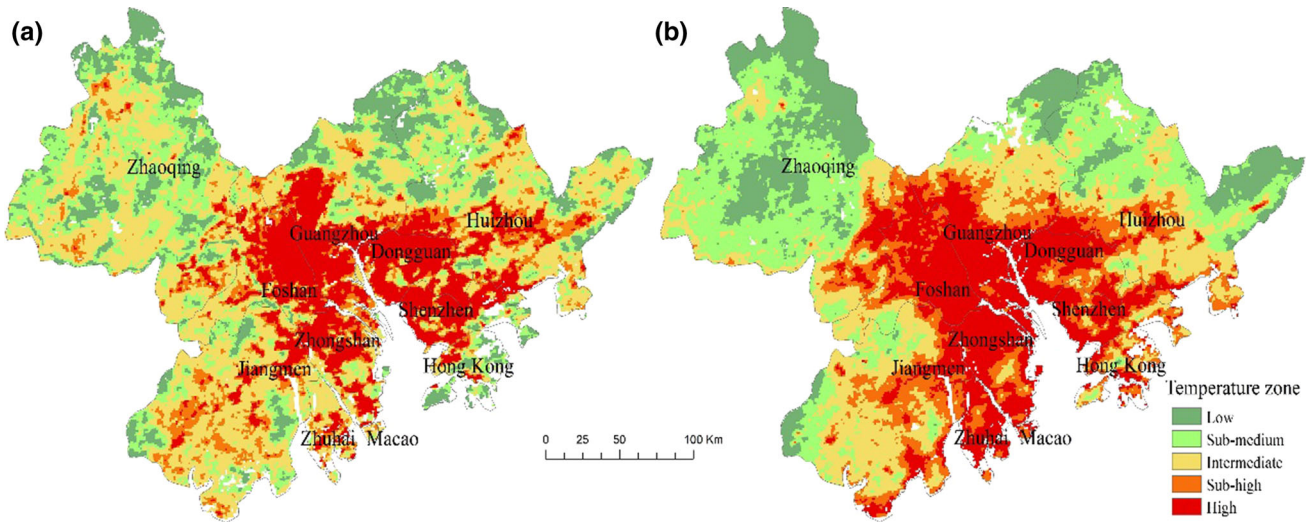

Fig. 7 LST classification map: **a** day, **b** night

respectively. When the ratio of short to long axis is greater than 1, the ellipse shows directivity, and the larger the ratio of long to short axis is, the more the directivity is. From the values in Table 8, the ratio of long to short axis of the three SDEs is all greater than 1, with obvious directivity. Among them, the ratio of daytime SDE (DTSDE) is 1.63, with the most obvious directivity, while the ratio of nighttime SDE (NTSDE) is small and the directivity is not obvious.

Correlation Analysis

LST Relationship with Different ISA Densities

We investigated the relationship between LST and LST, and the mean LST in the five ISA density areas was calculated. Table 9 shows that the ISA density has a significant and positive influence on the LST. And the highest value in LST can be found in the ISA areas with high density (33.66 °C in daytime and 25.17 °C in nighttime), the sub-medium-density area has the second highes LST value, and the lowest LST value is found in the low-density area of ISA. The temperature differences of LST between the high-density area and the low-density area during daytime and nighttime are 4.57 °C and 2.44 °C, respectively.

The Relationship Between LST and Landscape Metrics

The correlation coefficients between landscape metrics and LST are shown in Table 10, in which the LST is regional mean values in different ISA density areas. Overall, the

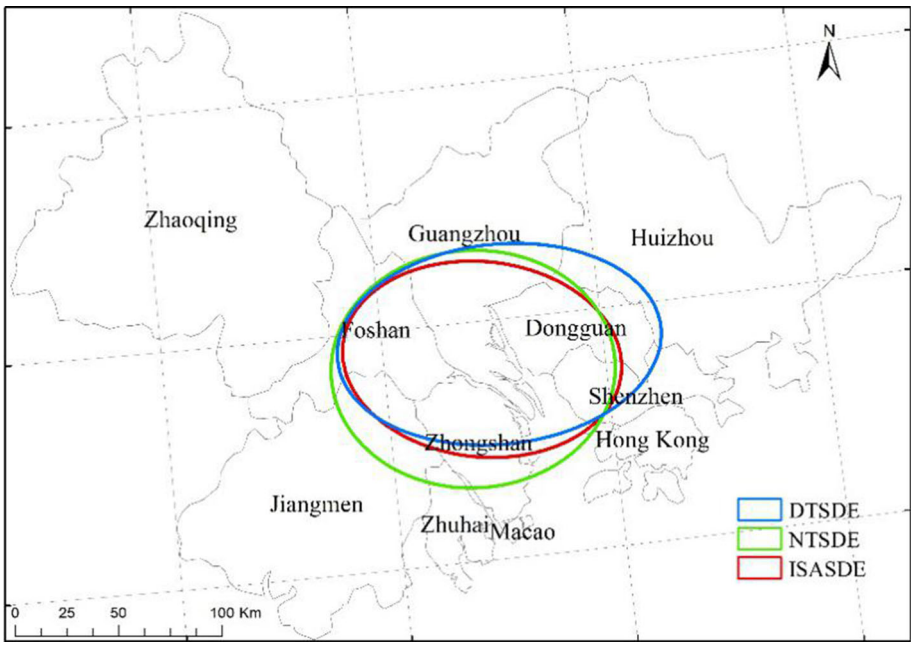

Fig. 8 SDE distribution map (DTSDE—daytime SDE; NTSDE—nighttime SDE; ISASDE—impervious surface SDE)

Table 8 SDE statistics table

	Long axis (km)	Short axis (km)	Direction angle	Long/short axis
ISASDE	65,076.26	45,372.57	101.24°	1.43
DTSDE	75,595.46	46,519.85	89.45°	1.63
NTSDE	66,072.22	55,182.18	92.77°	1.20

Table 9 LST statistics

Percent ISA	Daytime		Nighttime	
	LST (°C)	Temperature range (°C)	LST (°C)	Temperature range (°C)
Low-density area	29.09	0	22.73	0
Sub-medium-density area	30.40	1.31	23.67	0.94
Medium-density area	31.40	1.0	24.19	0.52
Secondary high-density area	32.60	1.2	24.68	0.59
High-density area	33.66	1.06	25.17	0.59

Table 10 Pearson correlation coefficients between LST and landscape metrics

	Daytime mean LST		Nighttime mean LST	
	R^2	P	R^2	P
NP	− 0.98	0.002	− 0.962	0.009
PD	− 0.98	0.002	− 0.962	0.009
LSI	− 0.85	0.067	− 0.788	0.113
PAFRAC	− 0.56	0.326	− 0.497	0.394
LPI	0.75	0.142	0.702	0.186
AREA_MN	0.88	0.05	0.841	0.074
AI	0.89	0.04	0.867	0.057
COHESION	0.97	0.004	0.982	0.003

landscape metrics had the stronger correlation with daytime LST than nighttime LST, excluding the COHESION. The patch structure metrics (AI and COHESION) and LST have strong and positive correlation, especially the COHESION metric. Moreover, the patch area metrics (LPI and AREA_MN) had positive correlation with the LST ($R^2 > 0.7$). In contrast, the patch density metrics (NP and PD) had a significant and negative correlation with the LST with R^2 of − 0.98 ($p = 0.002$) and − 0.96 ($p = 0.009$) in daytime and nighttime, respectively. Similarly, the patch shape metrics (LSI and PAFRAC) was negatively correlated with the LST.

Discussion

Influence of ISA Density on LST

We found the areas with the highest ISA density and LST are distributed in the middle cities of the GPRD during the daytime (Figs. 4a and 6). On the basis of trends in ISA, the LST demonstrated a progressive decline from the middle cities extends out into surrounding regions. It was preliminarily concluded that the density of ISA has an influence on the LST.

Table 9 indicates that the LST gradually increases with the increase in the ISA density in the day and night, which is consistent with the findings in the individual city or megacity scale (Weng and Lu 2008; Xian and Crane 2006; Weng et al. 2004, 2007). Furthermore, the calculation results show that when the ISA density increased 10%, the daytime LST increased 0.46 °C at the density level lower than 70% (low-density, sub-medium-density and medium-density areas) and 0.55 °C at the density level higher than 70% (sub-high- and high-density areas). Likewise, when the ISA density increased 10%, the nighttime LST increased 0.285 °C at the density level lower than 70% and 0.39 °C at the density level higher than 70%.

To further reveal the effect of ISA density on LST, we drew buffer zones every 15 km from the center to the edge of the GPRD and divided 96 zones in eight directions for spatial statistics (Fig. 1). The center selected in this study was the geographical center and the area with the highest density of ISA. Subsequently, the mean ISA density and LST of each zone are calculated. Using the buffer statistics method, the distribution characteristics of the ISA and the LST can be clearly expressed spatially. Moreover, the spatial correlation between the ISA and the LST was analyzed. The mean values of ISA density and LST in the zones are made into radar maps (Figs. 9 and 10). The comparison of ISA radar map and daytime radar map shows that the high values of ISA density and LST within 15–45 km occur in the north, west and southwest directions. In the 60 km and 75 km, the high ISA densities appear in the direction of the south and east. Meanwhile, the high LST values begin to appear in the south, southeast and east directions. The high values in the area of 90–120 km emerge in the east and southeast directions. Outside of 60 km, the low values of ISA density remain in the west, northwest, northeast and southwest directions. Meanwhile, the high values of LST never appear in the west, northwest, northeast and southwest directions outside the 45-km range. Compared with the ISA radar map and the nighttime radar map, the distribution of LST within 45 km has no obvious direction, while in the region beyond 60 km, the high values of LST remain in the south,

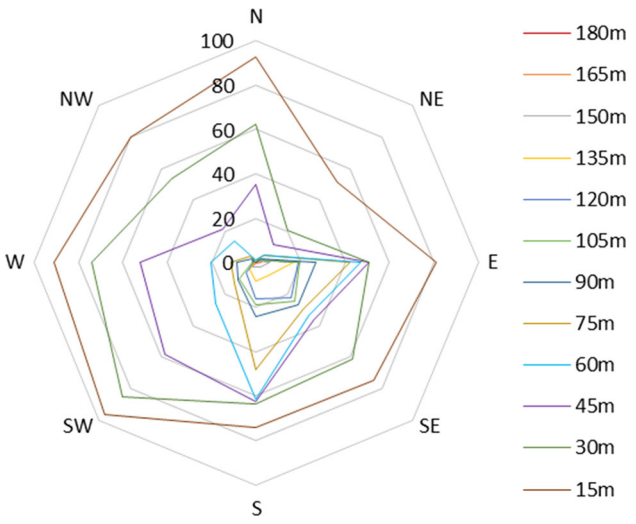

Fig. 9 ISA radar map

southeast and east directions all the time. In addition, the spatial distribution of LST was consistent with the ISA density. The radar maps show that in local space, the direction of ISA with the highest density has the highest LST. When the ISA density approaches 0, the corresponding LST has the lowest value in this region. It is also concluded that the ISA density has an effect on the LST, and the greater the ISA density per unit area, the higher the LST.

The radar maps show that the LST in the daytime changed significantly with the ISA density; furthermore, the temperature difference between high- and low-density areas of ISA was large. In contrast, in the nighttime, the LST did not change significantly with the density of the ISA, and the temperature difference is small. This phenomenon is caused by the ISA favors a strong absorption of solar radiation and considerably rapid warming of the high density of ISA during the day (Morabito et al. 2016). In addition, the study area was adjacent to the ocean, the LST in the low-density area decreases more slowly because of the influence of seawater insulation, so the high-temperature zone expands at night. From the point of view of the heat island effect, the high-density areas of ISA have a certain influence on the surrounding areas; in the meantime, the high LST radiates to the periphery. During the daytime, the high-density areas of the ISA heat up quickly, but at night, the LST around the high-density area of ISA is also relatively high due to the influence of radiation, so the temperature difference at night is relatively small.

The standard deviational ellipse explained some difference in the correlation between LST and ISA density during day and night (Fig. 8). The DTSDE is east–west, and the ISASDE is tilted with the northeast–southwest direction as the main axis, with certain differences. The

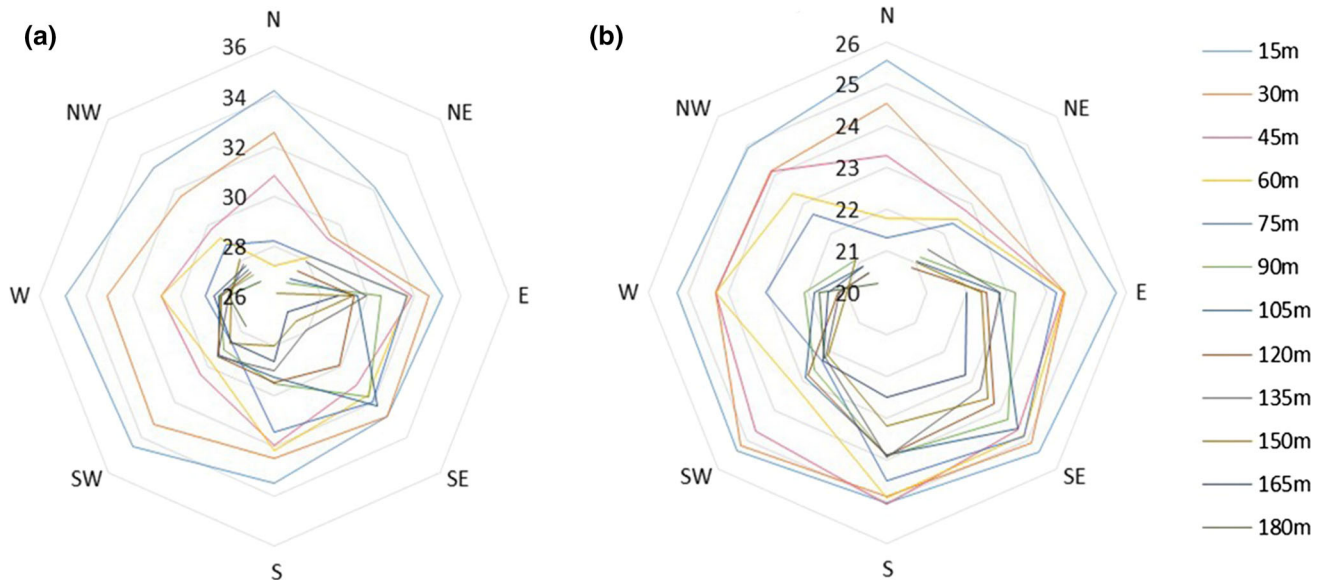

Fig. 10 LST radar map: **a** day, **b** night

Landsat 8 images showed that the difference was due to the distribution of bare land in Huizhou region in the east. The daytime LST strongly increased in the bare land due to solar radiation, which has a certain influence on the overall distribution of the LST, causing the DTSDE to shift. In contrast, the NTSDE has no obvious directivity. In addition, the range of the NTSDE is larger than that of ISASDE and DTSDE. The Landsat 8 image also shows a large number of paddy fields in Guangzhou, Zhongshan and Zhuhai. The LST was affected because the specific heat capacity of the water is large and the heat dissipation is slow; furthermore, the high-temperature zones were expanded. Therefore, the NTSDE has no obvious directionality.

To sum up, the high-temperature zones in the GPRD are mainly concentrated in cities like Foshan, Guangzhou, Dongguan, Shenzhen and Zhongshan. These cities are among the developed cities with the highest density of ISA in the GPRD, indicating that ISA density has an impact on LST. With the increase in ISA density, LST in daytime shows a gradually upward trend, and the LST in the area with the highest ISA density is the highest. Although the LST changes were not obvious in the nighttime, LST also remained high in the area covered by ISA.

Effect of Landscape Pattern on LST

The landscape metrics under five ISA density zones were calculated, and then the correlation analysis of landscape metrics and LST was conducted. The LST for daytime and nighttime was highly correlated with landscape metrics. The effect of landscape pattern of ISA on LST is explained in four aspects.

The patch density has a strong influence on LST. The patch density metrics (NP and PD) have a strong and negative correlation with the LST. The R^2 was -0.98 ($p = 0.002$) and -0.96 ($p = 0.009$) in daytime and nighttime, respectively. As the patch gradually aggregates, the total number of patches and the number of patches per unit area decrease. When the patch voids decrease, the land surface heat cannot diverge, causing the LST to rise.

The LST always rises with the change in the patch shape. The patch shape metrics (LSI and PAFRAC) are larger in the low-density area and minimum in the high-density area, while the LST is minimum in the low-density area and maximum in the high-density area. And the two metrics are negatively correlated with the LST, but the correlation between PAFRAC and LST is weak. The patches are fragmentation, complex shape and discrete distribution in the low-density area. However, in the high-density area, the patches have the strongest cohesion, better connectivity between patches. In addition, the patches shape is regular. The patch connectivity is enhanced, and the shape tends to be regular, which makes the surface heat dissipation slow.

In terms of patch area, the patch area metrics (LPI and AREA_MN) increased from low-density area to high-density area and reached the maximum in high-density area, showing a significant positive correlation with LST. With the increase in ISA density, not only the largest single patch area is increasing, but also the patch area within the unit area is also aggrandizing. As the patch area augments, the patches connect to each other, which slows down the heat dissipation. The higher the LST is, the more the patches with larger areas.

The patch structure has an effect on LST. The patch structure metrics (AI and COHESION) have a small value in the low-density area and the largest value in the high-density area. The patch structure metrics have a significant and positive correlation with LST. The COHESION has a great correlation with the LST; the R^2 reaches 0.97 ($p = 0.004$) and 0.98 ($p = 0.003$) during the daytime and nighttime, respectively. The patch distribution changes from dispersion to aggregation; the patch spatial continuity is enhanced; the dispersity is weakened; and the degree of polymerization increases. Therefore, the patch voids are reduced, so that the surface heat is unable to be released, causing the LST to rise.

However, besides COHESION, other landscape metrics and the correlation of the LST in the daytime than at night, landscape pattern has different effects on the LST of daytime and nighttime, due to the large terrain, complex environment and diverse surface cover types in the study area.

Overall, as the density of the ISA increases, the interstice between the patches continues to decrease and the number of patches continues to decrease. The patches appear to be continuous and cumulative, and the patch shape tends to be regular. This results in slow heat release from the ground and heat stored on the land surface, causing the LST to rise as the ISA changes. In general, larger, contiguous and regular patches produce higher LST than several smaller and dispersed patches.

Conclusions

In this study, the ISA of GPRD was extracted using Landsat 8 OLI. The MOD11A2 product was employed to investigate LST spatial distribution. Next, the SDE methods were used to systematically analyze the spatial correlation of ISA and LST at the whole region scales. Finally, the impact of ISA on LST at large scales of urban agglomerations was analyzed by a series of methods. The results show that the ISA of the GPRD was 9754.9362 km^2, accounting for 17.7% of the study area in 2015. Because of the rapid population and economic development level, the ISAs were aggregated in several cities: Foshan, Guangzhou, Dongguan, Zhongshan and Shenzhen. The annual average daytime LST was 22.68–37.56 °C, and the nighttime LST was 15.84–26.74 °C. Furthermore, the high-temperature zone of daytime LST was consistent with the ISA distribution. On the contrary, due to the influence of coastal water bodies and paddy fields at nighttime, the spatial extent of high-temperature zone of nighttime LST was larger than that of ISA and high-temperature zone of daytime LST. We found that this study highlights that the mean LST and the density of ISA had a significant and positive correlation in large-scale regions of urban agglomerations. When the ISA density increased 10%, the daytime LST increased 0.46 °C at the density level lower than 70% and 0.55 °C at the density level higher than 70%. Likewise, when the ISA density increased 10%, the nighttime LST increased 0.285 °C at the density level lower than 70% and 0.39 °C at the density level higher than 70%. Moreover, the landscape metrics of ISA showed a significant correlation with the LST, in which the patch density (NP and PD) had the strongest and negative correlation with the LST with an R^2 of − 0.98. In addition, the correlation between ISA and daytime LST or landscape metrics of ISA and daytime LST is stronger than that of nighttime LST due to the complexity of the urban agglomerations' topographical environment.

Overall, this study provides evidence of the effects of ISA density and landscape pattern on the LST in large-scale regions of urban agglomerations. On average, the mean LST of high-density area of ISA is higher than that of low-density area of ISA, and the LST of the patch of ISA with large area and better connectivity is higher than discrete patch of ISA, a compelling evidence for the temperature increase effect of high-density patch of ISA and spatial pattern of ISA. We suggest that compared to individual city, urban agglomerations need to pay more attention to the planning of ISA landscape pattern. We cannot reduce the number of ISA patches, but can add green spaces and water bodies to increase the interstice between the ISA, thus dispersing ISA structures. This can mitigate the LST and contribute to the sustainable development of the urban agglomerations.

Acknowledgements The authors would like to thank the anonymous reviewers and editor for constructive comments and suggestions.

Funding This work was supported by the Yunnan Normal University Postgraduate Innovation Fund [Grant Number yjs201680], Yunnan Provincial Department of Education Research Fund [Grant Number 2011Y307], National Natural Science Foundation of China [Grant Number 41461038], Yunnan Provincial Science and Technology Project [Grant Number 2011XX2005] and Specialized Research Fund for the Doctoral Program of Higher Education [Grant Number 20115303110002].

Compliance with Ethical Standards

Conflict of interest No potential conflict of interest was reported by the authors.

References

Alberti, M. (2005). The effects of urban patterns on ecosystem function. *International Regional Science Review, 28*(2), 168–192.

Chen, L., & Sun, R. (2013). Eco-environmental effects of urban landscape pattern changes: Progresses, problems, and perspectives. *Acta Ecologica Sinica, 33*(4), 1042–1050.

Chen, S., & Wang, T. (2009). Comparison analyses of equal interval method and mean-standard deviation method used to delimitate urban heat island. *Journal of Geo-information Science, 2,* 001.

Du, H., Wang, D., Wang, Y., Zhao, X., Qin, F., Jiang, H., et al. (2016). Influences of land cover types, meteorological conditions, anthropogenic heat and urban area on surface urban heat island in the Yangtze River Delta Urban Agglomeration. *Science of the Total Environment, 571,* 461–470.

Estoque, R. C., Murayama, Y., & Myint, S. W. (2017). Effects of landscape composition and pattern on land surface temperature: An urban heat island study in the megacities of Southeast Asia. *Science of the Total Environment, 577,* 349.

Fang, C. (2015). Important progress and future direction of studies on China's urban agglomerations. *Journal of Geographical Sciences, 25*(8), 1003–1024.

Fischer, M. M. (2010). Handbook of Applied Spatial Analysis. *Journal of Geographical Systems, 10*(2), 109–139.

Gong, J. (2002). Clarifying the standard deviational ellipse. *Geographical Analysis, 34*(2), 155–167.

Gong, A. D., Chen, Y. H., Jing, L. I., & Hua-Lang, H. U. (2007). Study on relationship between urban heat island and urban land use and cover change in Beijing. *Journal of Image and Graphics, 12,* 1476–1482.

Gustafson, E. J. (1998). Quantifying landscape spatial pattern: What is the state of the art? *Ecosystems, 1*(2), 143–156.

Huang, J., Zhao, X., Tang, L., & Qiu, Q. (2012). Analysis on spatiotemporal changes of urban thermal landscape pattern in the context of urbanisation: A case study of Xiamen City. *Shengtai Xuebao/Acta Ecologica Sinica, 32*(2), 622–631.

Jiang, X. D. (2007). Spatial characteristics and dynamic simulations of urban heat environment of cities in Pearl River Delta. *Acta Ecologica Sinica*, *27*(4), 1461–1470.

Jun Xiang, L. I., Wang, Y. J., Shen, X. H., & Song, Y. C. (2004). Landscape pattern analysis along an urban-rural gradient in the Shanghai metropolitan region. *Acta Ecologica Sinica, 24*(9), 1973–1980.

Kaloustian, N., & Diab, Y. (2015). Effects of urbanization on the urban heat island in Beirut. *Urban Climate, 14,* 154–165.

Kittler, J., & Illingworth, J. (1986). Minimum error thresholding. *Pattern Recognition, 19*(1), 41–47.

Lefever, D. W. (1926). Measuring geographic concentration by means of the standard deviational ellipse. *American Journal of Sociology, 32*(1), 88–94.

Li, J., Song, C., Cao, L., Zhu, F., Meng, X., & Wu, J. (2011). Impacts of landscape structure on surface urban heat islands: A case study of Shanghai. *China. Remote Sensing of Environment, 115*(12), 3249–3263.

Li, X., Zhou, W., Ouyang, Z., & Zheng, H. (2012). Spatial pattern of greenspace affects land surface temperature: Evidence from the heavily urbanized Beijing metropolitan area, China. *Landscape Ecology, 27*(6), 887–898.

Li, X., Zhou, W., & Ouyang, Z. (2013). Relationship between land surface temperature and spatial pattern of greenspace: What are the effects of spatial resolution? *Landscape and Urban Planning, 114*(8), 1–8.

Liu, Y., Peng, J., & Wang, Y. (2017). Relationship between urban heat island and landscape patterns: From city size and landscape composition to spatial configuration. *Acta Ecologica Sinica*, *37*(23), 1–12.

Lo, C. P., Quattrochi, D. A., & Luvall, J. C. (1997). Application of high-resolution thermal infrared remote sensing and GIS to assess the urban heat island effect. *International Journal of Remote Sensing, 18*(2), 287–304.

McGarigal, K., & Marks, B. J. (1995). FRAGSTATS: Spatial pattern analysis program for quantifying landscape structure. In *Genetics Technical Report PNW-GTR-351*. Portland, OR: US Department of Agriculture, Forest Service, Pacific Northwest Research Station.

McGarigal, K., Cushman, S. A., Neel, M. C., & Ene, E. (2002). Fragstats: spatial pattern analysis program for categorical maps. https://www.umass.edu/landeco/research/fragstats/fragstats.html.

Morabito, M., Crisci, A., Messeri, A., Orlandini, S., Raschi, A., Maracchi, G., et al. (2016). The impact of built-up surfaces on land surface temperatures in Italian urban areas. *Science of the Total Environment, 551–552,* 317–326.

Noro, M., & Lazzarin, R. (2015). Urban heat island in Padua, Italy: Simulation analysis and mitigation strategies. *Urban Climate, 14*(2), 187–196.

Peng, J., Liu, Y., Shen, H., Xie, P., Xiaoxu, H. U., & Wang, Y. (2016a). Using impervious surfaces to detect urban expansion in Beijing of China in 2000s. *Chinese Geographical Science, 26*(2), 229–243.

Peng, J., Xie, P., Liu, Y., & Ma, J. (2016b). Urban thermal environment dynamics and associated landscape pattern factors: A case study in the Beijing metropolitan region. *Remote Sensing of Environment, 173,* 145–155.

Rao, S., Zhang, H. Y., Jin, T. T., & Dou, H. Y. (2010). The spatial character of regional heat island in Pearl River Delta using MODIS remote sensing data. *Geographical Research, 29*(1), 127–136.

Rondeaux, G., Steven, M., & Baret, F. (1996). Optimization of soil-adjusted vegetation indices. *Remote Sensing of Environment, 55*(2), 95–107.

Roy, D. P., Wulder, M. A., Loveland, T. R., Woodcock, C. E., Allen, R. G., Anderson, M. C., et al. (2014). Landsat-8: Science and product vision for terrestrial global change research. *Remote Sensing of Environment, 145*(145), 154–172.

Runpeng, Z. (2013). Zhujiang delta spatial reorganization for new urbanization development. *Planners, 29*(4), 27–31.

Science (2016). Rise of the City. *Science*, *352*(6288), 906. https://doi.org/10.1126/science.352.6288.906.

Sun, R. (2012). How can urban water bodies be designed for climate adaptation? *Landscape and Urban Planning, 105*(1–2), 27–33.

Sungzoon, C., Robert, H., & Seungku, Y. (1989). Improvement of kittler and illingworth's minimum error thresholding. *Pattern Recognition, 22*(5), 609–617.

Turner, M. G. (2005). Landscape ecology: What is the state of the science? *Annual Review of Ecology Evolution and Systematics, 36*(36), 319–344.

Urban Agglomeration in the Pearl River Delta Yearbook (2016). (Vol. 2016). Guangzhou: Fangzhi Publishing House.

Wan, Z. (2008). New refinements and validation of the MODIS land-surface temperature/emissivity products. *Remote Sensing of Environment, 112*(1), 59–74.

Wan, Z., & Dozier, J. (1996). A generalized split-window algorithm for retrieving land-surface temperature from space. *IEEE Transactions on Geoscience and Remote Sensing, 34*(4), 892–905.

Weng, Q., & Lu, D. (2008). A sub-pixel analysis of urbanization effect on land surface temperature and its interplay with impervious surface and vegetation coverage in Indianapolis, United States. *International Journal of Applied Earth Observation and Geoinformation, 10*(1), 68–83.

Weng, Q., Lu, D., & Schubring, J. (2004). Estimation of land surface temperature–vegetation abundance relationship for urban heat island studies. *Remote Sensing of Environment, 89*(4), 467–483.

Weng, Q., Liu, H., & Lu, D. (2007). Assessing the effects of land use and land cover patterns on thermal conditions using landscape

metrics in city of Indianapolis. *United States. Urban Ecosystems, 10*(2), 203–219.

Wong, D. S. (1999). Several fundamentals in implementing spatial statistics in GIS: Using centrographic measures as examples. *Geographic Information Sciences, 5*(2), 163–174.

Wu, C. (2004). Normalized spectral mixture analysis for monitoring urban composition using ETM + imagery. *Remote Sensing of Environment, 93*(4), 480–492.

Xian, G., & Crane, M. (2006). An analysis of urban thermal characteristics and associated land cover in Tampa Bay and Las Vegas using Landsat satellite data. *Remote Sensing of Environment, 104*(2), 147–156.

Xu, H. (2009). Quantitative analysis on the relationship of urban impervious surface with other components of the urban ecosystem. *Acta Ecologica Sinica, 29*(5), 2456–2462.

Xu, H. Q. (2010). Analysis of impervious surface and its impact on urban heat environment using the normalized difference impervious surface index (NDISI). *Photogrammetric Engineering and Remote Sensing, 76*(5), 557–565.

Xu, H., & Chen, B. (2003). An image processing technique for the study of urban heat island changes using different seasonal remote sensing data. *Remote Sensing Technology and Application, 18*(3), 129–133.

Xu, S., Li, F. X., & Zhang, L. (2015). Spatiotemporal change of thermal environment landscape pattern in Changsha. *Acta Ecologica Sinica, 35,* 3743–3754.

Yue, W. Z., & Li-Hua, X. U. (2007). Thermal environment effect of urban land use type and pattern—A case study of central area of Shanghai City. *Scientia Geographica Sinica, 27*(2), 243–248.

Zhang, J. (2006). *Thermal environment detection in the Pearl River Delta Area by remote sensing and analysis of its spatial and temporal evolutions*. Ph. D. Dissertation, Guangzhou: Guangzhou Institute of Geochemistry, Chinese Academy of Sciences.

Zhang, Y., Yu, T., Gu, X., Zhang, Y., & Chen, L. (2006). Land surface temperature retrieval from CBERS-02 IRMSS thermal infrared data and its applications in quantitative analysis of urban heat island effect. *Journal of Remote Sensing, 10*(5), 789.

Zhang, L., Weng, Q., & Shao, Z. (2017a). An evaluation of monthly impervious surface dynamics by fusing Landsat and MODIS time series in the Pearl River Delta, China, from 2000 to 2015. *Remote Sensing of Environment, 201*(11), 99–114.

Zhang, S., Liu, Y., & Huang, H. (2017b). Research on quantitative evaluations and spatial and temporal distribution of heat islands for the Pearl River Delta agglomeration. *Ecology and Environmental Sciences, 26*(7), 1157–1166.

Zhang, S., Yang, K., Li, M., Ma, Y., & Sun, M. (2018). Combinational Biophysical Composition Index (CBCI) for effective mapping biophysical composition in urban areas. *IEEE Access, 6,* 41224–41237.

Zhao, Z.-Q., He, B.-J., Li, L.-G., Wang, H.-B., & Darko, A. (2017). Profile and concentric zonal analysis of relationships between land use/land cover and land surface temperature: Case study of Shenyang, China. *Energy and Buildings, 155,* 282–295.

Zheng, T., Lau, K. L., & Ng, E. (2016). Urban tree design approaches for mitigating daytime urban heat island effects in a high-density urban environment. *Energy and Buildings, 114,* 265–274.

Zhou, W., Huang, G., & Cadenasso, M. L. (2011). Does spatial configuration matter? Understanding the effects of land cover pattern on land surface temperature in urban landscapes. *Landscape and Urban Planning, 102*(1), 54–63.

Zhou, D., Dan, L., Ge, S., Zhang, L., Liu, Y., & Lu, H. (2016). Contrasting effects of urbanization and agriculture on surface temperature in eastern China. *Journal of Geophysical Research Atmospheres, 121*(16), 9597–9606.

Zhou, D., Bonafoni, S., Zhang, L., & Wang, R. (2018). Remote sensing of the urban heat island effect in a highly populated urban agglomeration area in East China. *Science of the Total Environment, 628–629,* 415–429.